High density amorphous ice at room temperature

Jing-Yin Chen and Choong-Shik Yoo[1]

Institute for Shock Physics and Department of Chemistry, Washington State University, Pullman, WA 99164–2816

Edited* by Russell J. Hemley, Carnegie Institution of Washington, Washington, DC, and approved March 23, 2011 (received for review January 14, 2011)

The phase diagram of water is both unusual and complex, exhibiting a wide range of polymorphs including proton-ordered or disordered forms. In addition, a variety of stable and metastable forms are observed. The richness of H_2O phases attests the versatility of hydrogen-bonded network structures that include kinetically stable amorphous ices. Information of the amorphous solids, however, is rarely available especially for the stability field and transformation dynamics—but all reported to exist below the crystallization temperature of approximately 150–170 K below 4–5 GPa. Here, we present the evidence of high density amorphous (HDA) ice formed well above the crystallization temperature at 1 GPa—well inside the so-called "no-man's land." It is formed from metastable ice VII in the stability field of ice VI under rapid compression using dynamic-diamond anvil cell (*d*-DAC) and results from structural similarities between HDA and ice VII. The formation follows an interfacial growth mechanism unlike the melting process. Nevertheless, the occurrence of HDA along the extrapolated melt line of ice VII resembles the ice Ih-to-HDA transition, indicating that structural instabilities of parent ice VII and Ih drive the pressure-induced amorphization.

dynamic-DAC | rapid solidication | high pressure kinetics | metastability

Abundant in nature, water is a major constituent of planets and living organisms alike. The phase diagram of water exhibits a large number of polymorphs with great diversity in crystalline structure, chemical bonding, and collective interactions (1–3). The hydrogen-bond angles and topology of relatively weak hydrogen bonds (with respect to covalent OH bonds) are subject to large distortions, which, in turn, lead to proton and structural disorders and myriad phases—both stable and metastable (including amorphous). In addition to a large number (approximately 15) of known solid phases of H_2O, there are many metastable phases. The metastable phases include both crystalline and disordered solids: high- and low-density amorphous (HDA and LDA) at low temperatures (4–11), high- and low-density water (HDW and LDW) (12), as well as crystalline phases of ice IV (13) near the melting line, VII (14) observed in the stability field of ice VI, VII′ (6, 15, 16) in the ice VIII stability field, and ice III in the ice II field (17). This is in addition to a whole series of intermediate structures arising from amorphorization, dipole-ordering transitions, and symmetrization of hydrogen bonding (4, 5, 18). The strength of hydrogen bonds varies in these metastable structures, as does the transition dynamics that is not well understood.

Recently, a very high density form of amorphous ice (VHDA) was found by isobaric annealing of HDA at 177 K and 1.9 GPa (7, 19). The presence of VHDA is characterized from HDA by its high density—not by the network structure. In fact, the VHDA is a topologically isomorphic phase to HDA, arising from the different interstitial occupancy of oxygen atoms. In this regard, there could be many intermediate structures "frozen in" along the movement of oxygen atoms (10), and a series of such high density amorphous ices (including e-HDA, u-HDA, and VHDA) can be viewed as a continuum of glasses (3, 10, 20). Nevertheless, the recent neutron diffraction studies (3) indicate that the phase behaviors of e-HAD and VHDA are rather distinctive.

The structure of ice VII consists of two interpenetrating hydrogen-bond networks (21). With increasing pressure, the nearest neighbor oxygen-oxygen distance in ice VII decreases, eventually bringing each of the hydrogen atoms to the midway points of the neighboring oxygen atoms (i.e., symmetrized ice-X) above 60–70 GPa (22). Above 150 GPa ice X further transforms to an antifluorite-like structure (23). At higher pressures, it is also predicted to transform to orthorhombic structures such as *Pbcm*, *Pbca*, and *Cmcm* (24). From 40–100 GPa, under increasing temperatures, ab initio molecular dynamics (MD) simulations have found evidence of enhanced hydrogen self-diffusion and significant ionic conductivity below the melting curve of H_2O (25, 26). Yet, with decreasing temperatures (below 270 K), hydrogen-disordered ice VII transforms to antiferroelectrically dipole-ordered ice VIII (27). Similarly, ice III transforms to dipole-ordered antiferroelectric ice IX below 170 K (28), and ice Ih to either antiferroelectric or ferroelectric ice XI below 70 K (29).

The proton- and dipole-ordering transitions in H_2O are governed by well beyond the thermodynamic constraints, to strong kinetics that gives rise to metastable structures as represented in Fig. 1. Neutron diffraction experiments and classical MD simulations (12, 30) provide evidence for the existence of two different liquids, LDW and HDW. This finding was later explained in terms of density fluctuation in liquid rather than a first-order phase transition in liquid (31). Under rapid "jet" cooling, water transforms into LDA, an amorphous solid, rather than ice Ih at the cooling rate of 10^6 K/s and at $T < 140$ K. Under low-temperature compression (below 150 K) LDA or ice Ih transforms to HDA, another amorphous solid (4–6). This transition was found to occur also to the extrapolated melting line of ice Ih and below the crystalline temperature of 150 K at 1 GPa; it was therefore called low-temperature "melting" of ice Ih (4, 5). This transition, at approximately 0.8–1 GPa and below 183 K, is accompanied by a large density increase due to the collapse of the second nearest oxygen neighbors into the first coordination shell (10, 11). For this reason, HDA and LDA are considered to be glassy forms of HDW and LDW and poorly collapsed crystalline phases, respectively. The absence of HDA at higher temperatures was attributed to a relaxation process that precluded HDA formation above the crystalline temperature. However, other studies examined the LDA-to-HDA transition from the standpoint of a mechanical instability of the ice I structure above 1 GPa (6, 8, 9). Indeed, the earlier studies (32, 33) pointed out that the two mechanisms are related in the pressure-induced amorphization of SiO_2. Subsequently, Strassle et. al. (34) found that the pressure-induced amorphization at low temperatures is due to mechanical melting, while amorphization at higher temperatures is dominated by thermal melting. The exact nature of these kinetically controlled phase boundaries among amorphous solids and liquids is not well understood.

Pressure-induced amorphization can be understood in terms of being controlled by thermodynamic principles, kinetics, mechanical or elastic instabilities, or combinations of these interrelated factors. Because framework structures are relatively strong, ice

Author contributions: C.-S.Y. developed the project, J.-Y.C. and C.-S.Y. designed research; J.-Y.C. performed research; J.-Y.C. and C.-S.Y. contributed new reagents/analytic tools; J.-Y.C. and C.-S.Y. analyzed data; and J.-Y.C. and C.-S.Y. wrote the paper.

The authors declare no conflict of interest.

*This Direct Submission article had a prearranged editor.

[1]To whom correspondence should be addressed. E-mail: csyoo@wsu.edu.

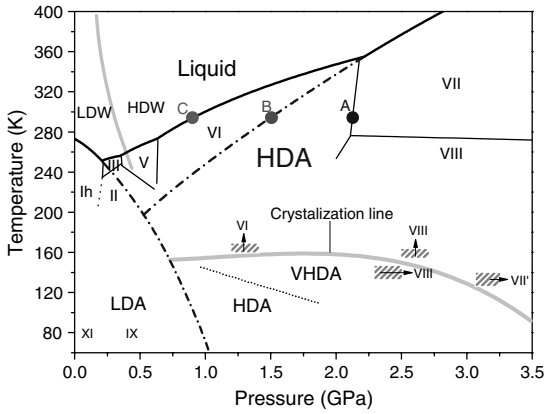

Fig. 1. The phase diagram of H_2O. The dashed-dotted curves are the extrapolated melting lines of ice Ih and ice VII to compare the pressure-induced amorphorization. The gray lines signify the proposed phase boundary of LDW and HDW (10) and the suggested crystallization line of amorphous ices (4, 6, 11). The HDA and VHDA phase boundary was reproduced from ref. 11. The hatch areas with arrows signify the crystallization of high density amorphous ice to various crystalline phases, reproduced from refs. 6 and 15.

can develop considerable lattice strain, inducing disorder at low temperatures. The apparent absence of HDA, VHDA, or any amorphous ice above the crystallization temperature (4–6), therefore, appears to advocate for thermal relaxation of this structural disorder in this no-man's land and implies that the first-order LDA-HDA/VHDA transition is governed by thermodynamic constraints rather than kinetics or mechanical instability. In contrast, we present experimental evidence for the existence of HDA arising from metastable ice VII in the stability field of ice VI at ambient temperature—well above the previously suggested crystallization temperature and only under rapid compressions. This kinetically controlled transition is due to structural similarities between supercompressed water (or HDW), ice VII, and HDA at pressures beyond the extrapolated melting line of ice VII (Fig. 1, *Inset*).

In this study, we employed a dynamic-DAC capable of precisely controlling sample pressures and compression rates (14, 35, 36) to search for any metastable structures, ordered or disordered, arising across the phase boundaries at room temperature. The samples were compressed to pressures between 1 and 4 GPa (Fig. 2) with a wide range of compression rates using a trapezoidal electrical pulse to three piezo-actuators. The phases and phase transitions were characterized by time-resolved changes of ruby fluorescence-based pressures, Raman characteristics, and microphotographic images of the sample—all

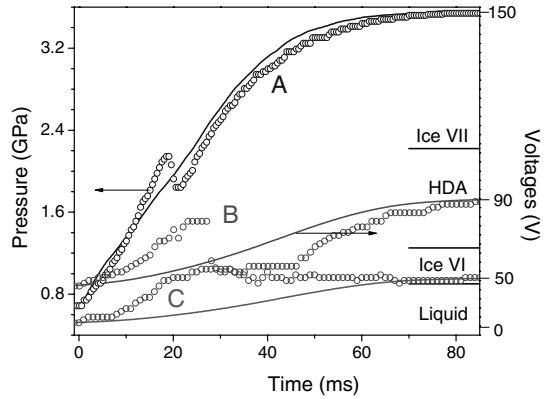

Fig. 2. The measured pressures of three typical experiments to the stability zones of ice VI (*C*), metastable ice VII where HDA forms (*B*), and ice VII (*A*), plotted together with the trapezoidal piezo-input signals. The labels on the right signify the pressure range observed the corresponding ice phases.

measured synchronously across the event of interest during compression and decompression cycles (Fig. 3).

Results and Discussion

Experimental evidence for the presence of HDA at ambient temperature was found in both the sample's water-like, untextured morphology and in the characteristic Raman spectrum (19, 37) at final pressures (or compression rates) above 1.3 GPa (or 0.1–65 GPa/s), as shown in Fig. 3. Starting pressures of all measurements were set to be around 0.5 GPa. At low compression rates (*C* in Figs. 1 and 2), water freezes into ice VI at the equilibrium pressure of 0.9 GPa with little or no pressure overshoot. At relatively higher compression rates (*A* or *B* in Figs. 1 and 2), water is supercompressed well above the equilibrium melt pressure to 2.1 GPa—the equilibrium phase VII and VI boundary pressure at ambient temperature—at which point it immediately transforms to ice VII with a substantial pressure drop. At these high compression rates, the presence of metastable ice VII is evident from its characteristic needle-like morphology (14) and from the Raman spectrum, as shown in Fig. 3. Following the large pressure drop, ice VII appears in the stability field of ice VI, as previously observed (14). Yet, we have found that this metastable ice VII transforms into HDA immediately after its rapid formation within 50 μs (see Fig. 4). Note in Fig. 3 that the Raman spectrum of the present HDA is quite similar to those of the previous observed HDA and VHDA at low temperatures (19, 37), considering the small temperature dependence in the HDA Raman spectrum (37). The Raman spectra of HDA are substantially broader than those of crystalline ice VI and VII. The ice VII to HDA transition is also evident from a plateau in the measured pressure (see the B record in Fig. 2), which indicates the coexistence of the two phases. In turn, the length of the pressure plateau represents the transition time of ice VII to HDA, which is confirmed by the framing record (Fig. 4*A*). Pressure again increases after the transition, following the rising part of the piezo-input; at this point, depending on the final pressure, the sample either changes to ice VII or remains in the HDA phase. The HDA remains as long as the pressure is between 2.1 GPa and 1.3 GPa. During decompression to pressures below 1.3 GPa, HDA transforms to ice VI (Fig. 4*B*), as evident from the granular shape and characteristic Raman. Then, ice VI melts to water at 0.9 GPa—the equilibrium melting pressure at ambient temperature.

Recall that the formation of HDA at low temperatures was described previously in terms of "melting" of ice Ih (4, 5). The transition of ice VII to HDA can be described as a similar melting process in the context of its morphology change as illustrated in Fig. 4 *A* and *B*; however, the growth mechanism seems to be quite different from the melting process. For example, the amorphization of ice VII (Fig. 4*A*) occurs within a few milliseconds over a large stability field of ice VI between 1.3 and 2.1 GPa, which indicates a kinetically controlled process. In contrast, the melting of ice VI (Fig. 4*B*) occurs much more slowly (several seconds) and always at the equilibrium melt pressure, indicating a thermal process. Therefore, we conclude that the Gibbs free energy difference drives the melting process. This is in contrast to the interfacial energy difference of the amorphization as described below.

The kinetic data based on the conversion rate of ice VII to HDA in Fig. 5 indicates that the ice VII-to-HAD transition is governed by two distinctive relaxation processes: slow ($\tau \sim$ tens of ms) below 1 GPa, and fast ($\tau <$ 1 ms) relaxation above 1 GPa. Note that the conversion rate of ice VII to HDA depends on the plateau pressure, not the rate of compression. This can be explained in terms of the displacive movement of oxygen atoms along an "idealized" crystallographic transition pathway. For example, ice VII has eight nearest oxygen atoms in its bcc-like structure, forming two different groups of tetrahedral oxygen atoms: one with hydrogen atoms between two adjacent oxygen atoms and

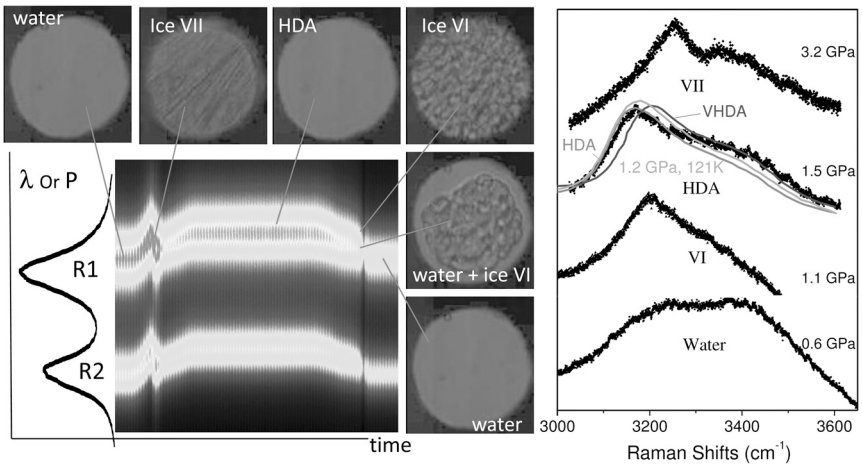

Fig. 3. (*Left*) The time-resolved ruby luminescence recorded on a 2D CCD as a function of wavelength (or pressure) and time, shown together with the selected real-time micro-photographic images distinctive to different phases of water and ice. The images were continuously recorded at the rate of 6,000 frames per second. (*Right*) The Raman spectra of liquid water, ice VI, HDA, and ice VII, obtained at the peak pressures of different experiments. The Raman spectra in the gray curves are reproduced from the references (19, 37), which was obtained at 1.2 GPa and 121 K, 1 atm and 80 K, and 1 atm and 80 K, respectively.

the other without. The oxygen-oxygen distance of ice VII is relatively incompressible, 2.95 Å at 1 GPa and 2.90 Å at 2 GPa; this is calculated based on the previously reported structure (38). On the other hand, HDA has only four nearest oxygen atoms at around 2.8 Å—nearly the same distance as that of ice VII, and 12 second-nearest neighbors at substantially larger distance at 3.7 Å at ambient pressure (11). Upon compression the first shell remains nearly unchanged, while the second collapses to 3.0 Å with five nearest neighbor atoms at 2 GPa (11). Therefore, the low-pressure transition to HDA requires the movement of four non-hydrogen bonded oxygen atoms from 2.95 Å to 3.7 Å along the body diagonal or the tetrahedral interstitial site of the bcc structure, which occurs slowly; whereas, at high pressures, the transition requires only a slight displacement of those oxygen atoms from 3.0 Å to 2.90 Å, which occurs rapidly. Thus, the transition of ice VII to HDA is clearly due to structural similarity (11).

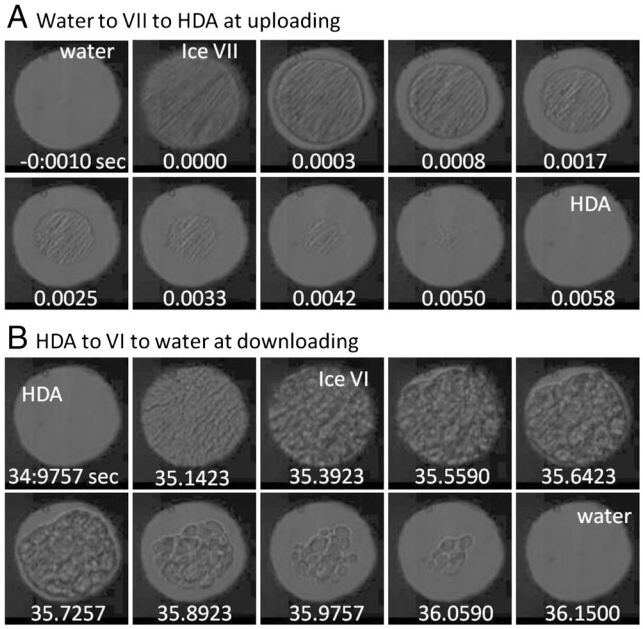

Fig. 4. High-speed microphotographic images of the sample showing (*A*) water solidification to ice VII and to HDA during rapid compression in comparison with (*B*) the transition of HDA to ice VI and then to liquid during rapid decompression.

Furthermore, the present transition mechanism is consistent with the previously suggested VHDA structure arising from the different interstitial occupancy (10).

Based on the transition state model (39), the activation volume $\Delta V^{\neq}$ can be estimated by $(\delta \ln k/\delta P)_T = -\Delta V^{\neq}/k_B T$, where k_B is Boltzmann's constant and T is temperature. From Fig. 5, we obtain two activation volumes associated with the ice VII to HDA transition: approximately -137 Å^3 below 1 GPa and 1.22 Å^3 above 1 GPa. These values can be compared with the volume differences between the first and second HDA shells. The volume differences were estimated using a spherical shell model and the neutron data (11): -97 Å^3 at pressures of 1.0–1.2 GPa and approximately 11 Å^3 between 1.2 and 2.1 GPa. These values are smaller than the activation volume changes as they should be, yet they are roughly in the same order.

In conclusion, we have observed HDA at room temperature, well beyond the previously suggested crystallization temperature of 150 K or "no-man's land" by dynamic loading (4–6). The fact that HDA forms from metastable ice VII in the stability field of ice VI indicates a kinetic control process, possibly by a low interface free energy. This is unlike the volume dependent free energy associated with melting process (4, 5). Therefore, we attribute the pressure-induced amorphization to the structural instability of the parent phases, ice VII and Ih. In contrast, the occurrence

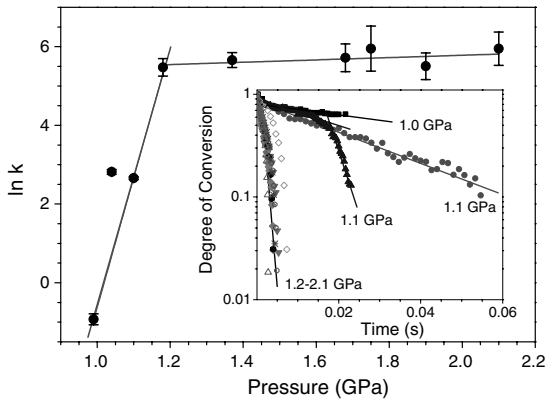

Fig. 5. The ice VII-to-HDA transition rate, k, plotted as a function of the plateau pressures, showing two distinctive relaxation mechanisms. The inset shows the degree of conversion, estimated from the measured volume changes associated with the ice VII to HDA transition, as a function of time. The slop represents the transition rate constant.

of HDA along the extrapolated melt line of ice VII (Fig. 1) resembles the ice Ih-to-HDA transition (4, 5), underscoring the fundamental role of mechanical instability in triggering the appearance of metastable structures within the Born criteria (6, 8, 9, 32, 33, 40, 41).

Materials and Methods

The detailed method of operating dynamic-DAC was described previously in refs. 14, 35, and 36. Our d-DAC is characterized by its compressive operation from the previous expansive one to adapt a standard DAC of piston-cylinder type. We employed the trapezoidal piezo-input pulse shape to maintain the flat top pressure to determine the kinetics at a constant load for a longer period time, whereas the previous one used the triangular pulse shape. It enables us to maintain the HDA phase for a longer time, which was missed in the previous study (14).

The sample preparation is similar to that of conventional DAC experiments. We loaded pure distilled water into a small (0.08–0.13 mm) hole in a preindented stainless steel gasket mounted between two diamond anvils (0.3 or 0.5 mm culets). We loaded all samples to a similar initial loading pressure of approximately $0.6(\pm 0.2)$ GPa in liquids nearby the freezing point of 0.8 GPa. The pressure of the sample was determined in real time by measuring time-resolved ruby luminescence (using 514.5 nm Ar^{+} excitation) at the rate of 1–1,000 spectra per second. Real-time sample images were also recorded using a high-speed camera (Photron FASTCAM APX RS) at the rate of 3,000–35,000 frames per second (Fig. 3, *Left*). The identity of ice phases was characterized by using the characteristic Raman spectra, synchronously obtained across the event of interest (Fig. 3, *Right*). We employed a home-built Raman/photographic imaging system, which shares the micro-focusing optics based on a long working distance objective (20x, Mitutoyo Ind.) and a confocal microscope system.

ACKNOWLEDGMENTS. The present study was performed in support of the National Science Foundation Division of Materials Research (0854618), American Chemical Society Petroleum Research Fund (49207-ND10), and US Department of Homeland Security under Award 2008-ST-061-ED0001. The views and conclusions contained in this document are those of the authors and should not be interpreted as necessarily representing the official policies, either expressed or implied, of the US Department of Homeland Security. Acknowledgment is made to the Donors of the American Chemical Society Petroleum Research Fund for partial support of this research.

1. Hemley RJ, et al. (1987) Static compression of H_2O-ice to 128 GPa (1.28 Mbar). *Nature* 330:737–740.
2. Soper AK (2002) Water and ice. *Science* 297:1288–1289.
3. Nelmes RJ, et al. (2006) Annealed high-density amorphous ice under pressure. *Nat Phys* 2:414–418.
4. Mishima O, Calvert LD, Whalley E (1984) 'Melting ice' I at 77 K and 10 kbar: A new method of making amorphous solids. *Nature* 310:393–395.
5. Mishima O, Calvert LD, Whalley E (1985) An apparently first-order transition between two amorphous phases of ice induced by pressure. *Nature* 314:76–78.
6. Hemley RJ, Chen LC, Mao HK (1989) New transformations between crystalline and amorphous ice. *Nature* 338:638–640.
7. Mishima O (1996) Relationship between melting and amorphization of ice. *Nature* 384:546–549.
8. Tse JS, et al. (1999) The mechanisms for pressure-induced amorphization of ice Ih. *Nature* 400:647–649.
9. Tse JS, Shpakov VP, Belosludov VR (1999) Vibrational spectrum, elastic moduli and mechanical stability in ice VIII. *J Chem Phys* 111:11111–11116.
10. Finney JL, et al. (2002) Structure of a new dense amorphous ice. *Phys Rev Lett* 89:205503.
11. Klotz S, et al. (2002) Structure of high-density amorphous ice under pressure. *Phys Rev Lett* 89:285502.
12. Saitta AM, Datchi F (2003) Structure and phase diagram of high-density water: The role of interstitial molecules. *Phys Rev E Stat Nonlin Soft Matter Phys* 67:020201.
13. Chou IM, Blank JG, Goncharov AF, Mao H-K, Hemley RJ (1998) In situ observations of a high-pressure phase of H_2O ice. *Science* 281:809–812.
14. Lee GW, Evans WJ, Yoo C-S (2006) Crystallization of water in a dynamic diamond-anvil cell: Evidence for ice VII-like local order in supercompressed water. *Phys Rev B Condens Matter Mater Phys* 74:134112.
15. Yoshimura Y, Mao H-k, Hemley RJ (2006) Direct transformation of ice VII′ to low-density amorphous ice. *Chem Phys Lett* 420:503–506.
16. Klotz S, et al. (1999) Metastable ice VII at low temperature and ambient pressure. *Nature* 398:681–684.
17. Bauer M, Winkel K, Toebbens DM, Mayer E, Loerting T (2009) Hexagonal ice transforms at high pressures and compression rates directly into "doubly metastable" ice phases. *J Chem Phys* 131:224514–224518.
18. Knight C, et al. (2006) Hydrogen bond topology and the ice VII/VIII and Ih/XI proton ordering phase transitions. *Phys Rev E Stat Nonlin Soft Matter Phys* 73:056113.
19. Loerting T, Salzmann C, Kohl I, Mayer E, Hallbrucker A (2001) A second distinct structural "state" of high-density amorphous ice at 77 K and 1 bar. *Phys Chem Chem Phys* 3:5355–5357.
20. Giovambattista N, Stanley HE, Sciortino F (2005) Phase diagram of amorphous solid water: Low-density, high-density, and very-high-density amorphous ices. *Phys Rev E Stat Nonlin Soft Matter Phys* 72:031510.
21. Kamb B, Davis BL (1964) Ice VII the densest form of ice. *Proc Natl Acad Sci USA* 52:1433–1439.
22. Benoit M, Marx D, Parrinello M (1998) Tunnelling and zero-point motion in high-pressure ice. *Nature* 392:258–261.
23. Loubeyre P, LeToullec R, Wolanin E, Hanfland M, Hausermann D (1999) Modulated phases and proton centring in ice observed by X-ray diffraction up to 170 GPa. *Nature* 397:503–506.
24. Militzer B, Wilson HF (2010) New phases of water ice predicted at megabar pressures. *Phys Rev Lett* 105:195701.
25. Cavazzoni C, et al. (1999) Superionic and metallic states of water and ammonia at giant planet conditions. *Science* 283:44–46.
26. Schwegler E, Galli G, Gygi F, Hood RQ (2001) Dissociation of Water under Pressure. *Phys Rev Lett* 87:265501.
27. Kuhs WF, Finney JL, Vettier C, Bliss DV (1984) Structure and hydrogen ordering in ices VI, VII, and VIII by neutron powder diffraction. *J Chem Phys* 81:3612–3623.
28. Londono JD, Kuhs WF, Finney JL (1993) Neutron diffraction studies of ices III and IX on under-pressure and recovered samples. *J Chem Phys* 98:4878–4888.
29. Tajima Y, Matsuo T, Suga H (1982) Phase transition in KOH-doped hexagonal ice. *Nature* 299:810–812.
30. Soper AK, Ricci MA (2000) Structures of high-density and low-density water. *Phys Rev Lett* 84:2881.
31. Clark GNI, Hura GL, Teixeira J, Soper AK, Head-Gordon T (2010) Small-angle scattering and the structure of ambient liquid water. *Proc Natl Acad Sci USA* 107:14003–14007.
32. Hemley RJ, Jephcoat AP, Mao HK, Ming LC, Manghnani MH (1988) Pressure-induced amorphization of crystalline silica. *Nature* 334:52–54.
33. Gregoryanz E, Hemley RJ, Mao H-k, Gillet P (2000) High-pressure elasticity of alpha -quartz: Instability and ferroelastic transition. *Phys Rev Lett* 84:3117–3120.
34. Strässle T, Klotz S, Hamel G, Koza MM, Schober H (2007) Experimental evidence for a crossover between two distinct mechanisms of amorphization in ice Ih under pressure. *Phys Rev Lett* 99:175501.
35. Evans WJ, et al. (2007) Dynamic diamond anvil cell (dDAC): A novel device for studying the dynamic-pressure properties of materials. *Rev Sci Instrum* 78:073904–073906.
36. Lee GW, Evans WJ, Yoo C-S (2007) Dynamic pressure-induced dendritic and shock crystal growth of ice VI. *Proc Natl Acad Sci USA* 104:9178–9181.
37. Salzmann CG, et al. (2006) Isobaric annealing of high-density amorphous ice between 0.3 and 1.9 GPa: In situ density values and structural changes. *Phys Chem Chem Phys* 8:386–397.
38. Fei Y, Mao H-K, Hemley RJ (1993) Thermal expansivity, bulk modulus, and melting curve of H_2O—ice VII to 20 GPa. *J Chem Phys* 99:5369–5373.
39. Evans MG, Polanyi M (1935) Some applications of the transition state method to the calculation of reaction velocities, especially in solution. *Trans Faraday Soc* 31:875–894.
40. Wang J, Li J, Yip S, Wolf D, Phillpot S (1997) Unifying two criteria of Born: Elastic instability and melting of homogeneous crystals. *Physica A* 240:396–403.
41. Cahn RW (2001) Materials science: Melting from within. *Nature* 413:582–583.